Graphene membranes with pyridinic-nitrogen at pore edges for high-performance CO_2 capture

Kuang-Jung Hsu[1], Shaoxian Li[1], Marina Micari[1], Heng-Yu Chi[1], Luis Francisco Villalobos[1,3], Shiqi Huang[1,4], Liping Zhong[2], Shuqing Song[1], Xuekui Duan[1], Andreas Züttel[2], Kumar Varoon Agrawal[1]*

[1] Laboratory of Advanced Separations (LAS), École Polytechnique Fédérale de Lausanne (EPFL), Rue de l'Industrie 17, CH-1951 Sion, Switzerland

[2] Laboratory of Materials for Renewable Energy (LMER), École Polytechnique Fédérale de Lausanne (EPFL), Rue de l'Industrie 17, CH-1951 Sion, Switzerland.

[3] Present address: Mork Family Department of Chemical Engineering and Materials Science, University of Southern California, Los Angeles, California, USA.

[4] Present address: Department of Chemical Engineering, University of Bath, Bath, UK

Abstract

Membranes based on a porous two-dimensional (2D) selective layer offer the potential to achieve exceptional performance to improve energy efficiency and reduce the cost for carbon capture. So far, separation from 2D pores has exploited differences in molecular mass or size. However, competitive sorption of CO_2 with the potential to yield high permeance and selectivity has remained elusive. Here, we show that a simple exposure of ammonia to oxidized single-layer graphene at room temperature incorporates pyridinic nitrogen at the pore edges. This leads to a highly competitive but quantitatively reversible binding of CO_2 with the pore. An attractive combination of CO_2/N_2 separation factor (average of 53) and CO_2 permeance (average of 10420) from a stream containing 20 vol% CO_2 is obtained. Separation factors above 1000 are achieved for dilute (~ 1 vol %) CO_2 stream, making the membrane promising for carbon capture from diverse point emission sources. Thanks to the uniform and scalable chemistry, high-performance centimeter-scale membranes are demonstrated. The scalable preparation of high-performance 2D membranes opens new directions in membrane science.

Introduction

Energy- and cost-efficient CO_2 separation technology are needed to improve the prospects of carbon capture.[1,2] High-performance membranes are promising to reduce the capture penalty (cost per unit CO_2 captured) from point emission sources because the membrane process does not rely on thermal energy. Developing CO_2-selective films with a high CO_2 permeance is an attractive strategy to reduce the needed membrane area and the corresponding capture penalty.[3] The state-of-the-art membranes based on polymer thin film composites,[4–6] metal-organic frameworks,[7,8] stacked nanosheet,[9] and layers facilitating CO_2 transport[10–12] have shown promising CO_2/N_2 separation performance. However, CO_2 permeance is bound by the thickness of the selective layer which is challenging to reduce below 50-100 nm while avoiding selectivity-deteriorating pinhole defects. 2D films hosting tailor-made pores have the potential to achieve high-performance membrane-based molecular separation,[13–19] and can mimic rapid and selective transport from the biological systems.[20,21] Porous single-layer graphene is an ideal 2D film for this purpose because the atom-thick pores in graphene minimize diffusional resistance for molecular transport.[22–25] Depending on the pore size, gas pair selectivity across a 2D pore can be determined by the impingement rate of molecules from the gas phase to the pore (effusion from large pores) or by the relative size of the molecules with

respect to the pore (steric transport regime from Å-scale pores).[26,27] Effusion from large pores yields extremely large permeance, however, the gas pair selectivity is capped by the mass ratio of molecules.[28,29] For Å-scale pores, gas pair selectivity is expected based on the relative differences in energy barrier that the molecule experiences during pore translocation.[26,27,30–32] While the size-dependent separation has been demonstrated to differentiate gas molecules with high selectivity,[23,33,34] however, it has proven extremely challenging to achieve both high selectivity and high gas permeance. This combination, if achieved, will improve the energy-efficiency of separation but also will reduce the needed membrane area and capital cost of the separation. Such a combination is attractive for many gas separations, and in particular, carbon capture where high CO_2 permeance along with a high CO_2/N_2 selectivity is highly desired.[3,11]

While 2D pores in graphene are ideally suited for ambitious high-performance carbon capture, a longstanding challenge in achieving this arises from difficulties in tightly controlling the pore size distribution in a scalable manner.[30] Herein, we develop a strategy for improving the carbon capture performance by increasing the binding affinity of CO_2 with the pore. This is achieved by heteroatomic doping of the pore edge resulting in a highly competitive sorption of CO_2 at the pore, consistent with theoretical predictions.[6,35,36] We introduce pyridinic N at the graphene pore edge to promote competitive CO_2 uptake via electrostatic interactions (Fig. 1a).[22,37,38] Pyridinic N has been reported to complex with CO_2 driven by the Lewis acid-base interaction which involves a donation of electron charge from N (Lewis base) to CO_2.[39,40] N at the pore edge was placed by reducing oxidized graphene film by NH_3 where a spontaneous N-H dissociation has been predicted to promote N doping in the lattice.[41] The incorporation of pyridinic N is confirmed by the emergence of N1s peak in the high-resolution X-ray photoelectron spectroscopy (XPS). Spontaneous but reversible uptake of atmospheric CO_2, in the form of complexed product, is observed. This is also corroborated by imaging pores using low-temperature scanning tunneling microscopy (LTSTM) where pores appear occupied and empty upon adsorption and desorption cycle, respectively. The high-affinity results in a high loading even from a dilute CO_2 feed which led to the realization of high CO_2 permeance as well as high CO_2/N_2 selectivity. Thanks to the scalable chemistry, high-performance from centimeter-scale membranes is demonstrated.

Synthesis and characterization of pyridinic-N-substituted graphene pores

Pores in single-layer graphene film were incorporated by controlled oxidation with O_3 (see methods for details).[42,43] Oxidation of graphene leads to the formation of O clusters surrounding the pores where the chemical identity of O is epoxy, ether, and semiquinone groups (Supplementary Fig. 1).[44–46] The latter is present solely at the pore edge restricted by the maximum number of covalent bonds for C atoms.[44] N was substituted at the pore edge by exposing oxidized graphene to NH_3 at 20 ºC for 24 h. This reaction proceeds with the reduction of semiquinone with NH_3 where an energetically favorable N-H dissociation in the presence of nucleophilic O leads to the bonding of N with the C edge (Supplementary Fig. 2).[41]

Characterization of the NH_3-treated sample with X-ray photoelectron spectroscopy (XPS) revealed the emergence of a broad N1s peak (Supplementary Fig. 3). Deconvolution of a high-resolution N1s spectrum (Fig. 1b) confirmed the incorporation of pyridinic (398.1 eV) and graphitic N (401.7 eV).[47,48] The incorporation of primary amine (-NH_2) was also observed (399.5 eV),[49] and is attributed to the ring-opening chemistry of NH_3 with the epoxy groups. Indeed, the incorporation of N was concomitant with the decrease in the concentration of epoxy and semiquinone functional groups (Supplementary Fig. 1).

The XPS data indicated that 9% of the sites in graphene were occupied by N. This amounts to an atom density of 3.8×10^{14} cm^{-2}. Further mass balance indicated that pyridinic N constitutes approximately 15%

of the total N sites (Supplementary Table 1 and 2), which makes pyridinic site density of 5.7×10^{13} cm^{-2}. Pyridinic N serves as a Lewis base and complexes with CO_2.[50] The $-NH_2$ sites chemisorb CO_2 forming carbamate ($-NHCOO^-$) and ammonium ($-NH_3^+$), and additionally HCO_3^- when adsorbed water is also present (Supplementary Note 1, Fig. 1a).[51,52] These CO_2-derivatives were also observed in the high-resolution N1s XPS spectrum of the sample exposed to the ambient atmosphere. The complexation product of CO_2 with pyridinic N (referred to hereafter as Py.CO_2) could be deconvoluted at 403.1 eV.[48] $-NHCOO^-$ (~400.5 eV)[49] and $-NH_3^+$ (~401.7 eV)[53] were also observed. HCO_3^- was observed from the C1s XPS spectrum (289.0 eV, Supplementary Fig. 4).[51,52] We note that the 400.5 eV peak can also be assigned to pyrrolic N,[54] however, a mass balance on the total density of $-NH_2$ and its derivatives ($-NHCOO^-$ and $-NH_3^+$) during sorption and desorption rules out a significant population of pyrrolic N. This is further confirmed by desorption at 400 ^oC (Supplementary Note 2 and Supplementary Table 2).

The complexation of CO_2 with the pyridinic N sites was quantitatively reversible. Py.CO_2 could be dissociated by heating the sample at 150 ºC for 60 min in the ultrahigh vacuum (UHV) chamber of XPS where a complete loss of the Py.CO_2 peak was observed (Fig. 2c, Supplementary Fig. 5). The population gain for the pyridinic N site was quantitatively similar to the population loss for Py.CO_2 (Fig. 2d). Heating also led to a decrease in the population of $-NHCOO^-$, $-NH_3^+$, and HCO_3^- (Supplementary Fig. 5 and 6). Again, population gain for $-NH_2$ sites was quantitatively similar to the loss of chemisorbed sites. These observations are consistent with the physisorption and the chemisorption of CO_2 with pyridinic N and $-NH_2$ sites, respectively.[55]

The adsorption of CO_2 on the pores could be visualized by imaging pores by LTSTM (Fig. 3a). For this, we incorporated pyridinic-N-substituted pores in atomically-smooth highly-oriented pyrolytic graphite (HOPG) substrate, by oxidizing HOPG followed by NH_3 treatment. We observed several clusters as bright features in the image (Fig. 3b). The clusters were 2-3 nm in size and had a density of 3.0×10^{12} cm^{-2}, comparable to the size and density of clusters on the oxidized lattice before the reaction with NH_3 (Supplementary Fig. 9). The clusters are generated during the oxidation of graphene and are composed of a honeycomb superstructure of cyclic epoxy trimers and semiquinone groups.[44] Upon reaction with NH_3, a fraction of the epoxy groups in the clusters is expected to be converted to $-NH_2$ by the ring-opening chemistry. On the other hand, part of the semiquinone groups in the clusters is expected to be converted into pyridinic-N groups (Supplementary Fig. 2). Interestingly, while a donut cluster morphology (circular clusters with a cavity in the center) is always observed before the reaction with NH_3 consistent with the existence of a pore in the center of the cluster,[44,46] we mostly observed filled clusters after the NH_3 treatment (Fig. 3b and c; Supplementary Fig. 9 and 10). A likely explanation is the masking of the pore cavity by Py.CO_2 from an unavoidable brief exposure of the sample to the atmosphere during sample preparation. To confirm this, we heated the sample to 150 ºC where Py.CO_2 is expected to be completely dissociated. Indeed, donut-shaped clusters hosting a cavity appeared after the heating step. To confirm whether this change in morphology was due to reversible CO_2 desorption or due to an irreversible cluster structure evolution, we exposed the cluster again to CO_2 and imaged the sample again. The majority of the clusters were found to be filled, which in combination with the XPS data (see below) confirms that pores were occupied by CO_2 (Fig. 3b, c).

The reversible adsorption and desorption of CO_2 on the pyridinic N substituted pores could also be demonstrated inside the UHV chamber of a near-ambient pressure (NAP) XPS (Fig. 3d-e, Supplementary Table 1). CO_2 adsorption was carried out by exposing the specimen to 20 mbar CO_2 at 30 ºC for 30 mins. The desorption experiment was carried out by heating the specimen in UHV at 150 ºC for 1 h. The repeated adsorption and desorption cycles reveal that CO_2 sorption was quantitatively reversible (Fig. 3d-e) where the total number of pyridinic N and $-NH_2$ sites were conserved. The increase in the density of Py.CO_2 during adsorption was in quantitative agreement with the decrease in the density of pyridinic N (Fig. 3f). We also

noted a similar quantitative trend in the opposite direction during desorption. This trend was also true for -NH_2 and its derivatives (-$NHCOO^-$ and -NH_3^+). Due to the absence of water in the UHV chamber, we did not observe the formation of HCO_3^-.

The incorporation of N in the graphene lattice was also confirmed by the energy-dispersive X-ray spectroscopy (EDS, Fig. 4a-b). EDS mapping shows that N functional groups are well distributed on the graphene lattice. O was also observed in the EDS and the XPS data, which can be attributed to the generation of the -OH group from the ring-opening chemistry of NH_3 and the epoxy group,[56] besides unreacted precursor O-functional groups (epoxy, ether, and semiquinone groups).

Raman spectroscopy (Fig. 4c) and mapping data (Supplementary Fig. 13 and 14) also confirmed the incorporation of pyridinic N in the graphene lattice (Fig. 4c).[57] The incorporation of the heteroatom in graphene lattice decreases the intensity ratio for the *2D* peak to the *G* peak (I_{2D}/I_G) and shifts the *G* peak position, w_G.[57–59] Indeed, we observed that I_{2D}/I_G ratio decreased from over 2 (pristine lattice) to less than 1 for the NH_3-treated graphene (Fig. 4d). This was concomitant with a blue shift in w_G. The shift increased when the density of pyridinic N was increased, i.e., by increasing the NH_3 reaction temperature to 80 ºC (Supplementary Fig. 15, Supplementary Note 3). These observations indicate that pyridinic N led to *p*-doping of the graphene lattice. The estimated change of Fermi energy is -155.6, and -226.0 meV for doping at 20 and 80 ºC, respectively (Supplementary Note 4, Supplementary Table 3).

The pores when visualized by 80 keV beam in aberration-corrected high-resolution transmission electron microscopy (AC-HRTEM, Supplementary Fig. 16) revealed functional groups surrounding the pores, consistent with the presence of clusters around the pore. The brightness of these groups can be attributed to the presence of N functional group (i.e., -NH_2 group) and O-functional groups on top of the carbon lattice.[46] The functional groups were stable in 80 keV beam, in contrast to the precursor epoxy clusters which rapidly gasify in the presence of the electron beam (Supplementary Fig. 17, Supplementary Movies 1 and 2),[46] indicating improved stability of N-substituted pores.

CO_2 transport and separation performance of graphene membrane

Given the high affinity of the pyridinic N with CO_2, we prepared pyridinic-N-substituted graphene membranes to study gas separation properties. Crack-free graphene film could be prepared using a mechanical reinforcement strategy with two different support films, a 100-nm-thick nanoporous carbon film (NPC) film (Supplementary Fig. 18), and 200-nm-thick polydimethylsiloxane (PDMS) film (Supplementary Fig. 19), to achieve high-quality membranes.[42,60] These support films were chosen because they possess a high CO_2 permeance. NPC film hosting 20-40 nm pores[61] yields a large gas flux ($> 2 \times 10^5$ GPU of CO_2 permeance with 0.8 of CO_2/N_2 selectivity) (Supplementary Fig. 18d), and therefore, it does not add significant resistance to the gas transport. Scalable, gas-phase reactants (O_3 for oxidation, NH_3 for pyridinic N substitution) allowed the preparation of centimeter-scale membranes on porous polymeric support (Fig. 4a, Supplementary Fig. 20-21) in addition to membranes on metal-foil support (see method).

NH_3 treatment was directly carried out on oxidized graphene resting on porous support which allowed us to probe the changes in the gas transport properties (mixed feed, 20 vol.% CO_2) after the NH_3 treatment (Fig. 5b-c, Supplementary Table 4). We exposed a highly oxidized graphene, yielding large CO_2 permeance (average of 47030 gas permeation units or GPU; 1 GPU = 3.35×10^{-10} mol m^{-2} s^{-1} Pa^{-1}) but with a moderate CO_2/N_2 separation factor (SF, average of 13.7), to NH_3 for 24 h. The resulting membrane yielded an improved CO_2/N_2 SF (average of 53.3) while yielding a high CO_2 permeance (average of 10420 GPU, Fig. 5c). This is attributed to the competitive binding of CO_2 to the pore leading to the formation of Py.CO_2 complex. The strong binding is expected to increase the residence time of CO_2 at the pore.[37] The

improvement in CO_2/N_2 selectivity followed the NH_3 exposure time, consistent with the expected increase in the density of pyridinic N with the reaction time (Fig. 5b-c). As a control, NH_3-treatment for the standalone support film without graphene was carried out. We did not observe any change in the gas transport behavior of the support film (Supplementary Fig. 22).

To further understand the effect of CO_2 sorption on membrane performance, we analyzed the saturation of pyridinic N sites as a function of CO_2 partial pressure, p, at 30 ºC by counting the density of Py.CO_2 complex using XPS. We observed a sharp increase in the loading of pyridinic N sites at a low p with coverage of 30 and 45% at p of 0.4 and 20 mbar, respectively, and a full site saturation at 1 bar (Supplementary Table 5). Fitting this data with the Langmuir adsorption model, an adsorption equilibrium constant, K_{eq}, of 4.4×10^{-4} Pa^{-1} is obtained, consistent with that in the literature on N-doped carbon[62,63] (Fig. 5d and Supplementary Note 5).

The sharp loading of CO_2 at low p is also reflected in the increasing CO_2 permeance at lower p (Fig. 5e and Supplementary Table 6). The CO_2 permeance was several-fold higher at low p compared to that at p of 1 bar. Our model on gas transport predicts the experimental data well (Fig. 5e and Supplementary Note 5). The sharp increase of CO_2 permeance at lower p is attributed to the strong CO_2 adsorption in the dilute condition leading to fast CO_2 transport. As a result of increasing permeance at low p, we could design membranes with high performance by controlling porosity in graphene using oxidation time (30 and 60 min). For membranes with high oxidation time (60 min), large CO_2 permeance (average of 33880 GPU) combined with high CO_2/N_2 SF (average of 150) could be obtained at p of 8.4 mbar (Fig. 5f). SF exceeding 1000 (average of 1428) could be obtained from graphene with a lower oxidation time (30 min) at p of 8.4 mbar (Fig. 5f). An example of such a membrane is shown in Fig. 5g with SF near 2585 and CO_2 permeance of 5900 GPU at p of 8.4 mbar.

The entire set of data from membranes prepared by low and high oxidation time could be modeled by taking into account the fraction of selective (Å-scale) pores, C_{py}, where gas transport is determined by the translocation coefficient across the pore[27], as well as nonselective (large) pores operating in the effusive regime.[29] The transport model predicts the variation in gas permeance as a function of C_{py} quite well, with higher porosity membranes susceptible to lower C_{py}, and therefore, lower selectivity (Fig. 6a, Supplementary Table 10).

Given a good prediction of the CO_2 permeance with our transport model, we extracted K_{eq} based on p-dependent permeation data at three different temperatures (20, 60, and 100 ºC, Supplementary Note 5, Supplementary Table 11). By plugging the temperature-dependent K_{eq} into Van 't Hoff equation, CO_2 binding energy of 0.26 eV was obtained (Supplementary Table 12), in agreement with the theoretical prediction for CO_2 complexation with pyridinic N in the range of 0.20-0.27 eV.[40,64]

To verify that gas transport was primarily from Å-scale pores, single component permeation of several gases (He, H_2, CO_2, N_2, and CH_4) at a feed pressure of 2 bar was carried out (Supplementary Fig. 27). Gas permeation at three different temperatures (30, 60, and 100 ºC) was probed. The permeance of all gases except CO_2 increased with temperature (Supplementary Fig. 28) indicating activated transport for these gases with apparent activation energy ($E_{act\text{-}app}$) in the range of 11-18 kJ $mole^{-1}$ (Fig. 6b, Supplementary Note 6). This confirms that a majority of the pores are small where the transport is determined by the energy barrier that the gas molecule experiences during translocation across the pore. For CO_2, as expected, due to the strong adsorption effect from complexation with pyridinic N, the transport was dominant by CO_2 adsorption, with $E_{act\text{-}app}$ close to zero (Fig. 6b).

The performance of the membrane can be predicted by a resistance transport model which shows that porous graphene film controls gas transport (Supplementary Fig. 29a). As a result, the separation performance of the graphene membranes prepared using two different support films (NPC and PDMS) was comparable (Supplementary Fig. 29b-30a). Given the high CO_2/N_2 separation performance, we probed the separation property of membranes for the postcombustion capture application using mixed feed with CO_2 concentration of 20 vol% using graphene prepared by high oxidation time. Based on data from several different membranes (Supplementary Fig. 30b), an average CO_2 permeance of 10420±1710 GPU and CO_2/N_2 SF of 53.3±9.8 could be obtained (Fig. 6c). This represents a significant improvement over the performance of the state-of-the-art membranes (Supplementary Table 13) based on polymer thin film composites,[1] stacked nanosheet,[9] and layers facilitating CO_2 transport,[5,10,12,65] especially considering the reduction of the capture penalty (see discussion later).

To understand the stability of the membrane, we carried out a prolonged permeation test of membranes using the mixed gas feed (20 vol% of CO_2 in N_2). For example, SF and CO_2 permeance from membranes prepared using NPC support film remained steady for several days (Fig. 6d). A slight decrease in permeance was observed, however, the permeance could be recovered by simply heating the module at 150 ºC for 30 min. The recovery of permeance indicates weak and reversible physisorption of contaminants, in contrast to the aging of carbon molecular sieves.[66] Similar trends were observed for membranes prepared using polymeric support films (Supplementary Fig. 31). XPS measurements confirmed that N-functional groups on the lattice are conserved after multiple cycles of heat treatment (Supplementary Fig. 32).

The attractive separation performance in this work can potentially reduce the carbon capture penalty from a range of point sources, including concentrated emissions from steel/cement plants (p of 200 mbar)[67] and coal-based power plants (p of 130-140 mbar).[68,69] The high-performance at dilute CO_2 concentration (Fig. 5f) is attractive for capture from aluminum production and natural gas combined cycle where p are 10–20, and 30–40 mbar, respectively.[70] A techno-economic analysis for carbon capture from these sources using a double-stage membrane process with CO_2 recovery and purity of 90 and 95%, respectively, was carried out (Supplementary Note 7). The analysis predicts a capture cost of 20 $/ton$_{CO2}$ for concentrated feed (p of 200 mbar), and 76 $/ton$_{CO2}$ for extremely dilute feed (p of 10 mbar). The attractive capture penalty for extremely dilute feed can be used to improve the CO_2 recovery (e.g., to 99%) which if otherwise emitted to the atmosphere increases the burden on the negative emission technologies.

Conclusion

Overall, we have developed highly selective 2D pores in graphene by incorporating functional heteroatoms at the pore edge, leading to improved separation performance compared to state-of-the-art membranes for carbon capture. Pyridinic-N-substituted graphene pores readily adsorb CO_2 even from a very dilute mixture, e.g., we observe the binding of atmospheric CO_2 with pyridinic N in XPS experiments. This high affinity combined with the 2D nature of the pores results in high permeance and high selectivity, a feat that can significantly reduce the capture penalty. The involved chemistry of graphene utilizes gaseous reactants, i.e., O_3 for oxidation and NH_3 for the incorporation of pyridine, and as a result, is intrinsically highly scalable and amenable for implementation in large area samples. This finding will not only inspire molecular simulations and experiments to screen the regimes of competitive sorption that can be applied to membranes but also to develop high-performance adsorbents, sensors, and catalysts.

Methods

Synthesis of porous graphene

Single-layer graphene films were synthesized on Cu foil by chemical vapor deposition (CVD) as reported before.[42] Pores in graphene were introduced by oxidation by reaction with O_3 gas (9 wt% O_3 on a molar basis) at 250 ºC for a total duration of 3s, as described before.[43] To further increase the porosity of the sample, the pores were slowly expanded in O_3 gas at 20 ºC for 30-60 min. Two sets of samples were prepared, one with low porosity (30 min expansion), and the other at high porosity (60 min).

Pyridinic-N-substituted graphene

For introducing pyridinic N at the pore edge, oxidized graphene was transferred to porous support (Supplementary Fig. 37). Briefly, the graphene film was spin-coated with three different support layers (NPC and PDMS). A solution of turanose and polystyrene-co-poly(4-vinyl pyridine) (PS-P4VP) was spin-coated on top of graphene on Cu (1000 rpm for 60s) for preparing NPC-reinforced graphene.[60] Subsequently, the film was pyrolyzed at 500 °C in the H_2/Ar environment. For polymeric support, the graphene film was spin-coated 4wt% PDMS solution in heptane (1000 rpm for 60 s). The PDMS solution was prepared by mixing 10 wt% PDMS in heptane using a commercial monomer and crosslinking agent (Slygard 184). A ratio of 11:1 was used for the monomer and the crosslinking agent. This solution was stirred for 4 h at 70 °C followed by dilution to 4 wt%. The resulting solution was spin-coated on porous graphene at 1000 rpm for 1 minute. After this, the sample was dried for 24 h at 60 °C. Pyridinic-N-substituted graphene membranes supported by polymeric film were prepared by removing the Cu foil and collecting the graphene film onto the porous support. The resulting graphene membranes were dried at 20 ºC for 24 h.

Following this, the Cu foil was removed by dissolving it in 1 M $FeCl_3$. The film was rinsed in a 1 M HCl bath for 1 h and a deionized water bath for 1 h, following which it was collected by porous support. Two different supports were used, (i) porous polybenzimidazole (PBI) support obtained by nonsolvent-induced phase separation (NIPS), and (ii) porous W foil support hosting 5 µm laser-drilled pores.[42] The former was solely used for membranes. The latter was used for XPS, Raman, and for membranes. Porous PBI support was fabricated by using a solution of commercial PBI (PBI-AM Fumion®) in N-methyl-2-pyrrolidone up to 8 wt% and casting a wet film using a doctor blade on a macroporous stainless-steel mesh (SSM, pore opening of 20 µm). Phase separation was carried out by dipping the casted film in water (60 ºC) which led to a film with 20 nm pores. The resulting film was calcinated at 500 ºC before use.

NH_3 treatment was directly carried out on oxidized graphene resting on the porous support. For this, oxidized graphene was placed into a conical flask containing 7 N NH_3 in methanol. The flask was sealed and pumped to remove air from the overhead space. The reaction was carried out at room temperature for up to 24 h. Additional samples for Raman spectroscopy and XPS were also prepared by carrying out the reaction at 80 ºC for 24 h. After the reaction time, the sample was placed into a vacuum at 25 ºC for 12 h and then in 1 bar Ar at 150 ºC to remove the residual solvent.

Material characterization

C1s and N1s XPS analysis as well as Raman analysis were conducted on graphene resting on W foil. For this, oxidized graphene graphene samples were coated with a 1.25 wt% PTMSP solution in toluene (1000 rpm for 30 s, and then 2000 rpm for 30 s)[42]. Following the NH_3 treatment as indicated above, pyridinic-N-substituted graphene was transferred to porous W foil. The samples were immersed into a toluene solution for 2 h to remove the PTMSP film, used to transfer graphene (see the previous section). The resulting film was treated with two more baths of toluene to remove traces of PTMSP (Supplementary Fig. 38). Samples

were subsequently dried at 150 °C in Ar environment. O1s XPS analysis was conducted on HOPG to avoid complications from residues on transferred graphene which often makes O1s analysis challenging.

For XPS (Axis Supra from Kratos Analytical), samples were electrically grounded to the sample stage inside the UHV chamber. Measurements were carried out using the monochromated Kα line of an aluminum X-ray source (1486.6 eV) with the analyzer set at a pass energy of 20 eV.

The in situ adsorption/desorption experiment was carried out inside a NAP-XPS (SPECS Surface Nano Analysis GmbH, Germany) equipped with a PHOIBOS-150 multichannel hemispherical electron energy analyzer coupled with a differentially pumped electrostatic pre-lens system. In situ adsorption experiment involved exposing 20 mbar of CO_2 to the sample cell at 30 °C inside the UHV chamber for 30 min. Following this, the chamber was evacuated, and XPS data was collected. Desorption was conducted by heating the samples inside the UHV chamber at 150 °C for 1 h. Additional experiments also used heating of samples in UHV chamber to up to 400 °C following which XPS data was measured. All the fitting of spectra was performed via CasaXPS software.

Raman measurement was carried out using Renishaw micro-Raman spectroscope equipped with a blue laser (λL = 457 nm, EL = 2.71 eV). Analysis of the Raman data was carried out in MATLAB. For the calculation of the *D*, *G*, and *2D* peak information, the background from the spectrum was subtracted using the least-squares curve fitting tool.

AC-HRTEM analysis was performed in a double-corrected Titan Themis 60 - 300 (FEI, Thermo Fisher Scientific) equipped with a Wein-type monochromator. As-synthesized CVD graphene was suspended on Au TEM grids hosted in 0.6 - 1.2 µm holes. This was carried out by the wet-transfer technique using paraffin as a support layer. Following this, paraffin was removed by immersing the grid in heptane leaving suspended graphene on the grid. Samples were annealed at 500 °C in a CO_2 atmosphere to remove contaminants that mask the graphene lattice.[71] The oxidation and NH_3 treatments were subsequently carried out on the graphene suspended on the grid using the protocol mentioned above. An 80 keV incident electron beam was used to inhibit the knock-on damage during acquisition. The high-pass and Gaussian filters were applied to AC-HRTEM images to reduce noise and improve contrast. HAADF-STEM images and EDS maps were collected using Tecnai Osiris at 80 kV on the Au grid.

FEI Teneo scanning electron microscope, operating with an acceleration voltage of 1 kV was used for observing the surface and the cross-section of the support films, including NPC and PDMS. Three samples were imaged to calculate the average and standard deviation of the film thickness.

The LTSTM (CreaTec Fischer & Co. GmbH) was conducted at 4 K using liquid He cryostats. The experiment is sensitive to surface roughness and contaminations, hence smooth and flat HOPG substrate was used to study the pore morphology. Prior to oxidation, HOPG was freshly cleaved to obtain a flat and smooth surface. The oxidation and NH_3 treatments were subsequently carried out using the protocol mentioned above. The STM tip was prepared by cutting a commercial Pt/Ir wire (Pt: 90 wt % and diameter of 0.25 mm; Alfa Aesar). The STM images were analyzed by using the WSXM software.[72]

Gas permeation experiment

Single component and mixed gas permeation tests were carried out in a homemade permeation module (Supplementary Fig. 39). The permeation setup was composed of pre-calibrated mass flow controllers (MFCs) and a mass spectrometer (MS, Hiden Analytical, HPR-20). The calibrations were performed within a 5% error. For all measurements, the permeate was swept with Ar (1 bar), which was then sent to MS for estimating the permeate concentration in real-time. Single component testing was carried out at a feed pressure of 2 bar. Mixture tests were carried out at variable feed pressure of 1.4 to 2 bar. Thermal annealing in CO_2 at 150 °C for 0.5 h before each measurement at 30 °C was carried out.

The permeance, $\boldsymbol{J_i}$, for gas, i is given by

$$J_i = Q_i/(A \cdot \Delta P_i) \quad (1)$$

where Q_i is the molar flow rate of gas i across the membrane, **A** is the active membrane area, and ΔP_i is transmembrane pressure difference for the component i. The ideal selectivity of two gases, i and k, was calculated by dividing the permeance of gas i by the permeance of gas k. For the mixture gas permeation tests, the separation factor of two gases, i and k, was calculated using equation (2).

$$\alpha_{ik} = \frac{\left(\frac{c_i}{c_k}\right)_{permeate}}{\left(\frac{c_i}{c_k}\right)_{feed}} \quad (2)$$

Data availability

The datasets are available in the article, Supplementary Information, and the Source Data file.

Acknowledgment

The authors acknowledge the host institution EPFL for generous support. K.V.A. is thankful to GAZNAT for funding the project. K.V.A. would also like to thank Swiss National Science Foundation Assistant Professor Energy Grant (PYAPP2_173645), European Research Council Starting Grant (805437-UltimateMembranes), and Swiss National Science Foundation Project (200021_192005) for funding parts of this project. K.-J.H. would like to thank the joint EPFL-Taiwan Scholarship program for the Ph.D. grant.

Author Contributions Statement

K.V.A. and K.-J.H. conceived the project and wrote the manuscript. K.-J.H. prepared the samples for the membrane testing, XPS, Raman, SEM, HRTEM, and STM. K.-J.H. and L.Z. performed the XPS measurement. K.-J.H., H.-Y.C., and X.D. collected SEM data. H.-Y.C. and L.F.V. collected the AC-HRTEM images. K.-J.H. carried out the modeling of the transport. S.L. collected the STM data. K.-J.H., S. H., and S.S. developed support layers. M.M. performed the techno-economic analysis. All authors discussed the results and commented on the manuscript.

Competing Interests Statement

A patent application (European Patent Application EP22206687 (2022)) based on the findings of the work has been filed.

Figure Legends/Captions

Fig. 1. Uptake of CO_2 on pyridinic-N-substituted graphene. (a) Schematic illustration of pyridinic N at pore edge and -NH_2 near pore edge and binding of these groups with CO_2. In the schematic, the graphene lattice consists of carbon atoms shown in brown, with pyridinic nitrogen (blue atoms) substituted at the pore edges, primary amine groups (light blue) near the edges of the pores, and graphitic nitrogen (purple atoms) incorporated into the lattice. CO_2 molecules are depicted by two red and white atoms, adsorbed onto the graphene lattice.

Fig. 2. (a) N1s XPS spectrum of graphene hosting pyridinic N, -NH_2 and the corresponding derivatives from binding with CO_2. (b) Peak shift in N1s XPS after 150 ºC heating. (c) The density of various functional groups before and after 150 ºC heating. The desorption leads to the population gain for -NH_2 and pyridinic N but population loss for -$NHCOO^-$, -NH_3^+, and Py.CO_2. This relative change in density of the functional groups after the 150 ºC heating is shown in panel (d). The details of XPS fitting for (a) and (b) can be found in Supplementary Note 1.

Fig. 3. Quantitatively reversible CO_2 sorption on pyridinic-N-substituted graphene. (a) Schematic illustration of CO_2 desorption and adsorption on the pore. In the schematic, the CO_2 molecule is depicted by two red and white atoms, adsorbed onto the graphene lattice. The lattice itself is composed of carbon atoms represented in brown, with pyridinic nitrogen atoms (blue) at the pore edges, primary amine groups (light blue) near the edges, and graphitic nitrogen atoms (purple) incorporated in the lattice structure. (b) STM images, and (c) the 3D topography STM images of the occupied, empty, and re-occupied pores during sorption cycles. The yellow-colored region corresponds to higher elevations in the 3D topography, contrasting with the purple region, which represents lower elevations. The STM imaging was conducted on pyridinic-N-substituted HOPG (also see Supplementary Fig. 11). NAP-XPS data-based evolution of N functional groups with analysis of -NH_2 and relative derivatives in (d) and pyridinic N and Py.CO_2 in (e). The data "total" refers to the sum of -NH_2 and its derivatives in (d) and the sum of pyridinic N and Py.CO_2 in (e). (f) Percentage increase and decrease in the density of each functional group during sorption cycles.

Fig. 4. Confirmation of N functional groups in pyridinic-N-substituted graphene by EDS and Raman. (a) EDS mapped high-angle annular dark-field (HAADF) STEM images showing the distribution of C, N, and O. (b) A representative EDS spectrum showing the incorporation of N in the graphene lattice. (c) Raman spectrum of pristine graphene and pyridinic-N-substituted graphene (NH_3-treatment at 20 and 80 ºC). (d) I_{2D}/I_G versus *G* peak position, and (e) *2D* peak position versus *G* peak position. The dotted lines with arrows in (d) and (e) guide the change of the Raman spectrum with doping level.

Fig. 5. CO_2 adsorption and gas transport properties of pyridinic-N-substituted graphene. All data is based on graphene reinforced by NPC support film. (a) Picture of the centimeter-scale pyridinic-N-substituted graphene membrane. The edges of graphene on NPC support are highlighted by dotted orange lines. b-c) The improvement in transport properties of porous graphene after reaction with NH_3 at 20 ºC. The reaction time is 1.5 h in (b) and 24 h in (c). The graphene was etched with a high oxidation time (60 min) for (b) and (c). The error bars refer to the standard deviation in the separation factor and permeance across five, three, and six graphene membranes before and after 1.5 and 24 h N-substitution, respectively. The center of each error bar represents the average separation factor and permeance calculated from the graphene membranes. The permeation data is for mixed gas (20% CO_2) in N_2. (d) Py.CO_2 coverage extracted from XPS results and compared with sorption-based Langmuir model fitting (equation 2 in Supplementary Note 5). (e) The evolution of CO_2 permeance as a function of CO_2 partial pressure in feed, *p*. The dashed line is the prediction from the gas transport model (equation 6 in Supplementary Note 5). (f) CO_2/N_2 separation performance of membranes. Two sets of samples are prepared, one with a high oxidation time (60 min) and the other with a low oxidation time (30 min). The measurement was carried out at 12 and 8.4 mbar of CO_2 partial pressure. The error bars represent the standard deviation in the separation factor and permeance across graphene membranes. For membranes prepared at 12 mbar, data from ten membranes subjected to low oxidation time and five membranes subjected to high oxidation time are shown. For membranes

prepared at 8.4 mbar, standard deviations were calculated from seven membranes subjected to low oxidation and three membranes subjected to high oxidation. The center of each error bar represents the average separation factor and permeance calculated from the graphene membranes. (g) CO_2/N_2 separation performance of centimeter-scale membrane at *p* of 12 and 8.4 mbar. The permeation temperature for the entire set of data in this figure was 30 ºC.

Fig. 6. Competitive CO_2 adsorption led to attractive carbon capture performance from pyridinic-N-substituted graphene. All data is based on graphene reinforced by NPC support film. (a) CO_2 permeance (left axis) and CO_2/N_2 SF (right axis) as a function of the fraction of size-sieving pyridinic-N-substituted pores, C_{py}. The measurement is carried at *p* of 12 mbar. A high goodness of fitting ($R^2 > 0.99$) for CO_2 permeance versus C_{py} indicates that CO_2 transport is determined by the fraction of size-sieving pyridinic-N-substituted pores. The fraction of size-sieving pores is controlled by different oxidation times (30 or 60 mins). (b) The apparent activation energy for gases for translocating 2D pores, was extracted from the gas permeation data using the Arrhenius relationship. The green and green dash lines with arrows indicate the differences between the apparent activation energy for CO_2 and N_2. (c) Comparison of the CO_2/N_2 mixture separation performance with the state-of-the-art membranes for postcombustion capture. The error bars refer to the standard deviation in the separation factor and permeance across six membranes. The center of each error bar represents the average separation factor and permeance calculated from the graphene membranes. (d) Stability test of pyridinic-N-substituted graphene membrane with mixed feed (20 vol% of CO_2 in N_2) showing stable performance. The membrane was heated in the module at 150 ºC for 30 min to recover its permeance. Permeation temperature was 30 ºC in panels c and d. The graphene was oxidized with a high oxidation time (60 min).

References

1. Merkel, T. C., Lin, H., Wei, X. & Baker, R. Power plant post-combustion carbon dioxide capture: An opportunity for membranes. *J. Memb. Sci.* **359**, 126–139 (2010).
2. Han, Y. & Ho, W. S. W. Design of Amine-Containing CO2-Selective Membrane Process for Carbon Capture from Flue Gas. *Ind. Eng. Chem. Res.* **59**, 5340–5350 (2020).
3. Micari, M., Dakhchoune, M. & Agrawal, K. V. Techno-economic assessment of postcombustion carbon capture using high-performance nanoporous single-layer graphene membranes. *J. Memb. Sci.* **624**, 119103 (2021).
4. Pang, R., Chen, K. K., Han, Y. & Ho, W. S. W. Highly permeable polyethersulfone substrates with bicontinuous structure for composite membranes in CO2/N2 separation. *J. Memb. Sci.* **612**, 118443 (2020).
5. Zhang, Z., Rao, S., Han, Y., Pang, R. & Ho, W. S. W. CO2-selective membranes containing amino acid salts for CO2/N2 separation. *J. Memb. Sci.* **638**, 119696 (2021).
6. Fu, Y. *et al.* Ultra-thin enzymatic liquid membrane for CO2 separation and capture. *Nat. Commun.* **9**, 990 (2018).
7. Ghalei, B. *et al.* Enhanced selectivity in mixed matrix membranes for CO2 capture through

efficient dispersion of amine-functionalized MOF nanoparticles. *Nat. Energy* **2**, 17086 (2017).

8. Qiao, Z. *et al.* Metal-induced ordered microporous polymers for fabricating large-area gas separation membranes. *Nat. Mater.* **18**, (2018).

9. Zhou, F. *et al.* Ultrathin graphene oxide-based hollow fiber membranes with brush-like CO2-philic agent for highly efficient CO2 capture. *Nat. Commun.* **8**, 2107 (2017).

10. Chen, T.-Y., Deng, X., Lin, L.-C. & Ho, W. S. W. New sterically hindered polyvinylamine-containing membranes for CO2 capture from flue gas. *J. Memb. Sci.* **645**, 120195 (2022).

11. Han, Y. & Ho, W. S. W. Mitigated carrier saturation of facilitated transport membranes for decarbonizing dilute CO2 sources: An experimental and techno-economic study. *J. Membr. Sci. Lett.* **2**, 100014 (2022).

12. Marius, S. *et al.* An integrated materials approach to ultrapermeable and ultraselective CO2 polymer membranes. *Science* **376**, 90–94 (2022).

13. Moreno, C. *et al.* Bottom-up synthesis of multifunctional nanoporous graphene. *Science* **360**, 199–203 (2018).

14. Zeng, Y. *et al.* Irreversible synthesis of an ultrastrong two-dimensional polymeric material. *Nature* **602**, 91–95 (2022).

15. Jeon, M. Y. *et al.* Ultra-selective high-flux membranes from directly synthesized zeolite nanosheets. *Nature* **543**, 690–694 (2017).

16. Lin, L. C. & Grossman, J. C. Atomistic understandings of reduced graphene oxide as an ultrathin-film nanoporous membrane for separations. *Nat. Commun.* **6**, (2015).

17. Sun, P. Z. *et al.* Limits on gas impermeability of graphene. *Nature* **579**, 229–232 (2020).

18. Kidambi, P. R., Chaturvedi, P. & Moehring, N. K. Subatomic species transport through atomically thin membranes: Present and future applications. *Science* **374**, eabd7687 (2021).

19. Turchanin, A. & Gölzhäuser, A. Carbon Nanomembranes. *Adv. Mater.* **28**, 6075–6103 (2016).

20. Epsztein, R., DuChanois, R. M., Ritt, C. L., Noy, A. & Elimelech, M. Towards single-species selectivity of membranes with subnanometre pores. *Nat. Nanotechnol.* **15**, 426–436 (2020).

21. Tu, Y. M. *et al.* Rapid fabrication of precise high-throughput filters from membrane protein nanosheets. *Nat. Mater.* **19**, 347–354 (2020).

22. Jiang, D., Cooper, V. R. & Dai, S. Porous graphene as the ultimate membrane for gas separation. *Nano Lett.* **9**, 4019–24 (2009).

23. Koenig, S. P., Wang, L., Pellegrino, J. & Bunch, J. S. Selective molecular sieving through porous graphene. *Nat. Nanotechnol.* **7**, 728–732 (2012).

24. Surwade, S. P. *et al.* Water desalination using nanoporous single-layer graphene. *Nat. Nanotechnol.* **10**, 459–464 (2015).

25. Cheng, C., Iyengar, S. A. & Karnik, R. Molecular size-dependent subcontinuum solvent permeation and ultrafast nanofiltration across nanoporous graphene membranes. *Nat. Nanotechnol.* **16**, 989–995 (2021).

26. Wang, L. *et al.* Fundamental transport mechanisms, fabrication and potential applications of nanoporous atomically thin membranes. *Nat. Nanotechnol.* **12**, 509–522 (2017).

27. Yuan, Z. *et al.* Mechanism and Prediction of Gas Permeation through Sub-Nanometer Graphene Pores: Comparison of Theory and Simulation. *ACS Nano* **11**, 7974–7987 (2017).

28. Thiruraman, J. P. *et al.* Gas flow through atomic-scale apertures. *Sci. Adv.* **6**, 4–11 (2020).

29. Celebi, K. *et al.* Ultimate permeation across atomically thin porous graphene. *Science* **344**, 289–92 (2014).

30. Villalobos, L. F., Babu, D. J., Hsu, K., Van Goethem, C. & Agrawal, K. V. Gas Separation Membranes with Atom-Thick Nanopores: The Potential of Nanoporous Single-Layer Graphene. *Accounts Mater. Res.* **3**, 1073–1087 (2022).

31. Blankenburg, S. *et al.* Porous graphene as an atmospheric nanofilter. *Small* **6**, 2266–2271 (2010).

32. Sun, C., Wen, B. & Bai, B. Application of nanoporous graphene membranes in natural gas processing: Molecular simulations of CH4/CO2, CH4/H2S and CH4/N2 separation. *Chem. Eng. Sci.* **138**, 616–621 (2015).

33. Yuan, Z. *et al.* Direct Chemical Vapor Deposition Synthesis of Porous Single-Layer Graphene Membranes with High Gas Permeances and Selectivities. *Adv. Mater.* **2104308**, 2104308 (2021).

34. Sun, P. Z. *et al.* Exponentially selective molecular sieving through angstrom pores. *Nat. Commun.* **12**, 7170 (2021).

35. McDonald, T. M. *et al.* Cooperative insertion of CO2 in diamine-appended metal-organic frameworks. *Nature* **519**, 303–308 (2015).

36. Carreon, M. A., Li, S., Falconer, J. L. & Noble, R. D. Alumina-supported SAPO-34 membranes for CO2/CH4 separation. *J. Am. Chem. Soc.* **130**, 5412–5413 (2008).

37. Luan, B. *et al.* Crown Nanopores in Graphene for CO 2 Capture and Filtration. *ACS Nano* **16**, 6274–6281 (2022).

38. Wu, T. *et al.* Fluorine-Modified Porous Graphene as Membrane for CO2/N2 Separation: Molecular Dynamic and First-Principles Simulations. *J. Phys. Chem. C* **118**, 7369–7376 (2014).

39. Lim, G., Lee, K. B. & Ham, H. C. Effect of N-Containing Functional Groups on CO2 Adsorption of Carbonaceous Materials: A Density Functional Theory Approach. *J. Phys. Chem. C* **120**, 8087–8095 (2016).

40. Zhao, Y., Liu, X., Yao, K. X., Zhao, L. & Han, Y. Superior Capture of CO2 Achieved by Introducing Extra-framework Cations into N-doped Microporous Carbon. *Chem. Mater.* **24**, 4725–4734 (2012).

41. Wang, W. W., Dang, J. S., Zhao, X. & Nagase, S. Formation Mechanisms of Graphitic-N: Oxygen Reduction and Nitrogen Doping of Graphene Oxides. *J. Phys. Chem. C* **120**, 5673–5681 (2016).

42. Huang, S. *et al.* Millisecond lattice gasification for high-density CO 2 - and O 2 -sieving nanopores in single-layer graphene. *Sci. Adv.* **7**, eabf0116 (2021).

43. Hsu, K.-J. *et al.* Multipulsed Millisecond Ozone Gasification for Predictable Tuning of Nucleation and Nucleation-Decoupled Nanopore Expansion in Graphene for Carbon Capture. *ACS Nano* **15**, 13230–13239 (2021).

44. Li, S. *et al.* Structure Evolution of Graphitic Surface upon Oxidation: Insights by Scanning Tunneling Microscopy. *JACS Au* **2**, 723–730 (2022).

45. Lee, W. *et al.* Enhanced Water Evaporation from Å-Scale Graphene Nanopores. *ACS Nano* **16**, 15382–15396 (2022).

46. Huang, S. *et al.* In Situ Nucleation-decoupled and Site-specific Incorporation of Å-scale Pores in Graphene Via Epoxidation. *Adv. Mater.* 2206627 (2022) doi:10.1002/adma.202206627.

47. Li, X. *et al.* Simultaneous Nitrogen Doping and Reduction of Graphene Oxide. *J. Am. Chem. Soc.* **131**, 15939–15944 (2009).

48. He, W., Jiang, C., Wang, J. & Lu, L. High-rate oxygen electroreduction over graphitic-N species exposed on 3D hierarchically porous nitrogen-doped carbons. *Angew. Chemie - Int. Ed.* **53**, 9503–9507 (2014).

49. Compton, O. C., Dikin, D. A., Putz, K. W., Brinson, L. C. & Nguyen, S. T. Electrically conductive 'alkylated' graphene paper via chemical reduction of amine-functionalized graphene oxide paper. *Adv. Mater.* **22**, 892–896 (2010).

50. Lim, C.-H., Holder, A. M. & Musgrave, C. B. Mechanism of Homogeneous Reduction of CO2 by Pyridine: Proton Relay in Aqueous Solvent and Aromatic Stabilization. *J. Am. Chem. Soc.* **135**, 142–154 (2013).

51. Lao, M. *et al.* Platinum/Nickel Bicarbonate Heterostructures towards Accelerated Hydrogen Evolution under Alkaline Conditions. *Angew. Chemie - Int. Ed.* **58**, 5432–5437 (2019).

52. Bezerra, D. P. *et al.* CO 2 adsorption in amine-grafted zeolite 13X. *Appl. Surf. Sci.* **314**, 314–321 (2014).

53. Navaee, A. & Salimi, A. Efficient amine functionalization of graphene oxide through the Bucherer reaction: an extraordinary metal-free electrocatalyst for the oxygen reduction reaction. *RSC Adv.* **5**, 59874–59880 (2015).

54. Tian, K. *et al.* Single-site pyrrolic-nitrogen-doped sp 2-hybridized carbon materials and their pseudocapacitance. *Nat. Commun.* **11**, 2–11 (2020).

55. Choi, S., Drese, J. H. & Jones, C. W. Adsorbent materials for carbon dioxide capture from large anthropogenic point sources. *ChemSusChem* **2**, 796–854 (2009).

56. Vacchi, I. A., Spinato, C., Raya, J., Bianco, A. & Ménard-Moyon, C. Chemical reactivity of graphene oxide towards amines elucidated by solid-state NMR. *Nanoscale* **8**, 13714–13721 (2016).

57. Johns, J. E. & Hersam, M. C. Atomic covalent functionalization of graphene. *Acc. Chem. Res.* **46**, 77–86 (2013).

58. Wang, Q. H. *et al.* Understanding and controlling the substrate effect on graphene electron-transfer chemistry via reactivity imprint lithography. *Nat. Chem.* **4**, 724–732 (2012).

59. Ferrari, A. C. & Basko, D. M. Raman spectroscopy as a versatile tool for studying the properties of graphene. *Nat. Nanotechnol.* **8**, 235–46 (2013).

60. Huang, S. *et al.* Single-layer graphene membranes by crack-free transfer for gas mixture separation. *Nat. Commun.* **9**, 2632 (2018).

61. Dakhchoune, M. *et al.* Rapid Gas Transport from Block-Copolymer Templated Nanoporous Carbon Films. *Ind. Eng. Chem. Res.* **60**, 16100–16108 (2021).

62. Wang, Z. *et al.* N-doped porous carbon derived from polypyrrole for CO2 capture from humid flue gases. *Chem. Eng. J.* **396**, 125376 (2020).

63. Yang, C. *et al.* Facile preparation of N-doped porous carbon from chitosan and NaNH2 for CO2 adsorption and conversion. *Chem. Eng. J.* **432**, 134347 (2022).

64. Jiao, Y., Zheng, Y., Smith, S. C., Du, A. & Zhu, Z. Electrocatalytically Switchable CO2 Capture: First Principle Computational Exploration of Carbon Nanotubes with Pyridinic Nitrogen. *ChemSusChem* **7**, 435–441 (2014).

65. Datta, S. J. *et al.* Rational design of mixed-matrix metal-organic framework membranes for molecular separations. *Science* **376**, 1080–1087 (2022).

66. Jones, C. W. & Koros, W. J. Carbon molecular sieve gas separation membranes-II. Regeneration following organic exposure. *Carbon* **32**, 1427–1432 (1994).

67. Baker, R. W., Freeman, B., Kniep, J., Huang, Y. I. & Merkel, T. C. CO2 Capture from Cement Plants and Steel Mills Using Membranes. *Ind. Eng. Chem. Res.* **57**, 15963–15970 (2018).

68. Roussanaly, S., Anantharaman, R., Lindqvist, K., Zhai, H. & Rubin, E. Membrane properties required for post-combustion CO2 capture at coal-fired power plants. *J. Memb. Sci.* **511**, 250–264 (2016).

69. Giordano, L., Roizard, D., Bounaceur, R. & Favre, E. Evaluating the effects of CO2 capture benchmarks on efficiency and costs of membrane systems for post-combustion capture: A parametric simulation study. *Int. J. Greenh. Gas Control* **63**, 449–461 (2017).

70. Wang, X. & Song, C. Carbon Capture From Flue Gas and the Atmosphere: A Perspective. *Frontiers in Energy Research* vol. 8 (2020).

71. Villalobos, L. F. *et al.* Polybenzimidazole copolymer derived lacey carbon film for graphene transfer and contamination removal strategies for imaging graphene nanopores. *Carbon* **173**, 980–988 (2021).

72. Horcas, I. *et al.* WSXM: A software for scanning probe microscopy and a tool for nanotechnology. *Rev. Sci. Instrum.* **78**, 13705 (2007).

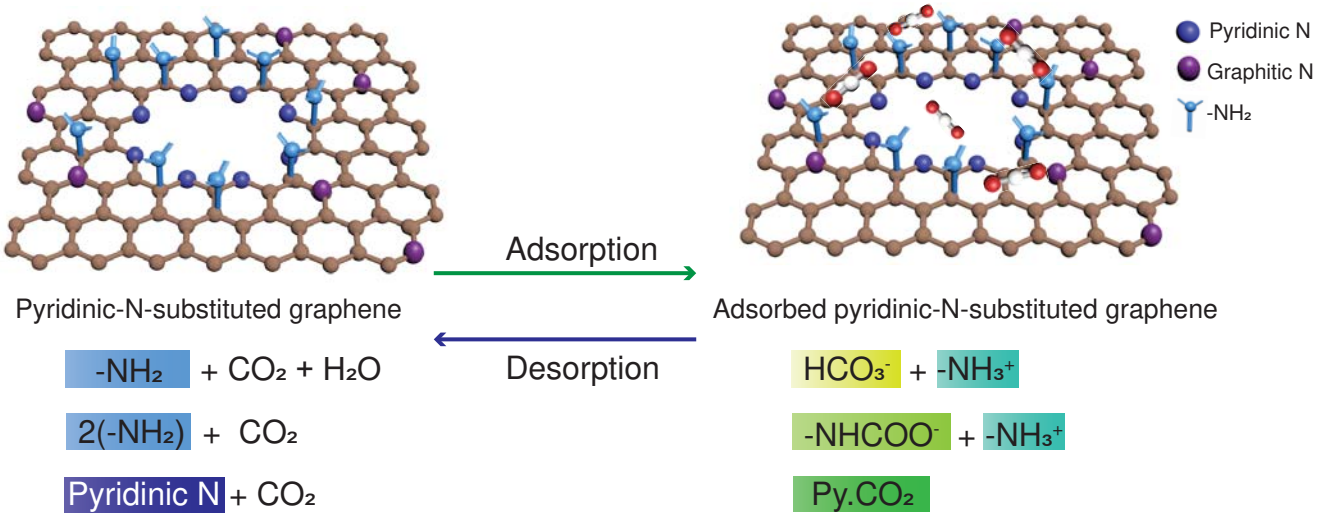
Pyridinic N
Graphitic N
-NH₂
Adsorption
Desorption
Pyridinic-N-substituted graphene
Adsorbed pyridinic-N-substituted graphene
-NH₂ + CO₂ + H₂O
HCO₃⁻ + -NH₃⁺
2(-NH₂) + CO₂
-NHCOO⁻ + -NH₃⁺
Pyridinic N + CO₂
Py.CO₂

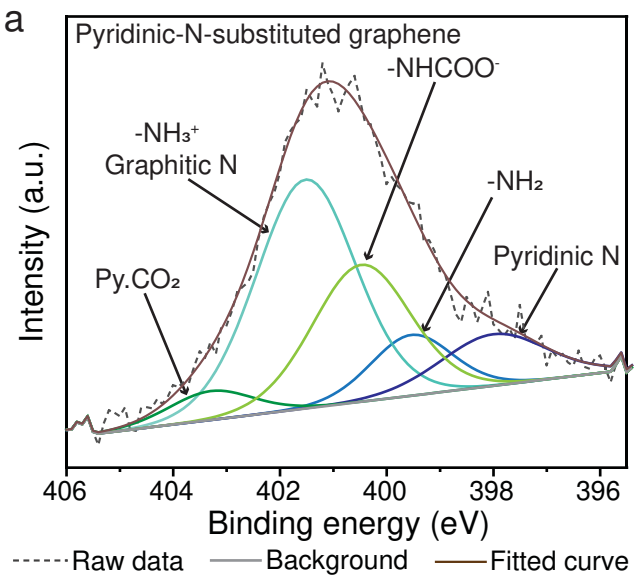
a
Pyridinic-N-substituted graphene
-NHCOO⁻
-NH₃⁺
Graphitic N
-NH₂
Pyridinic N
Py.CO₂
Intensity (a.u.)
406
404
402
400
398
396
Binding energy (eV)
Raw data
Background
Fitted curve

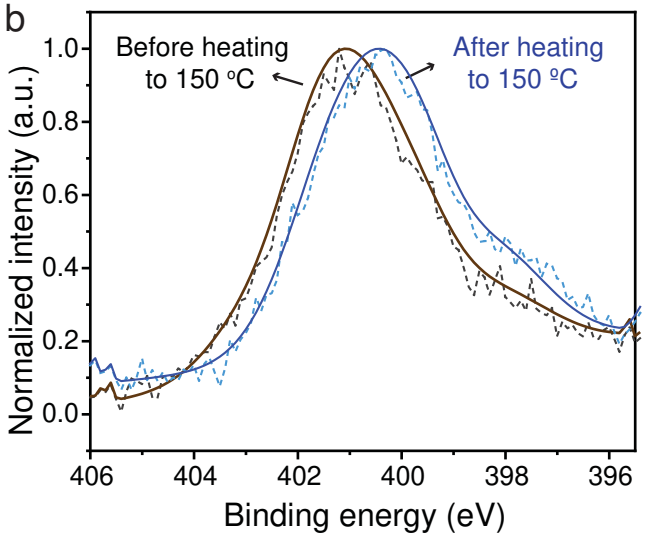
b
Before heating to 150 °C
After heating to 150 °C
Normalized intensity (a.u.)
1.0
0.8
0.6
0.4
0.2
0.0
406
404
402
400
398
396
Binding energy (eV)

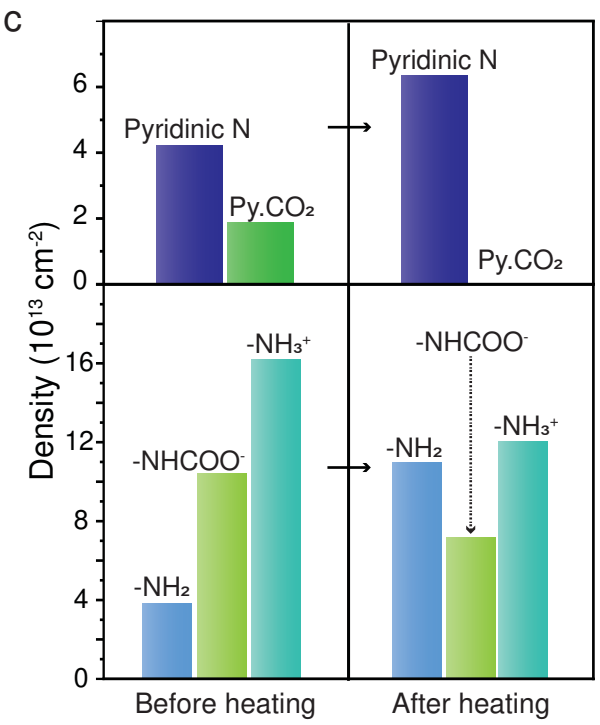
c
Pyridinic N
Py.CO₂
Density (10¹³ cm⁻²)
-NH₃⁺
-NHCOO⁻
-NH₂
Before heating
After heating

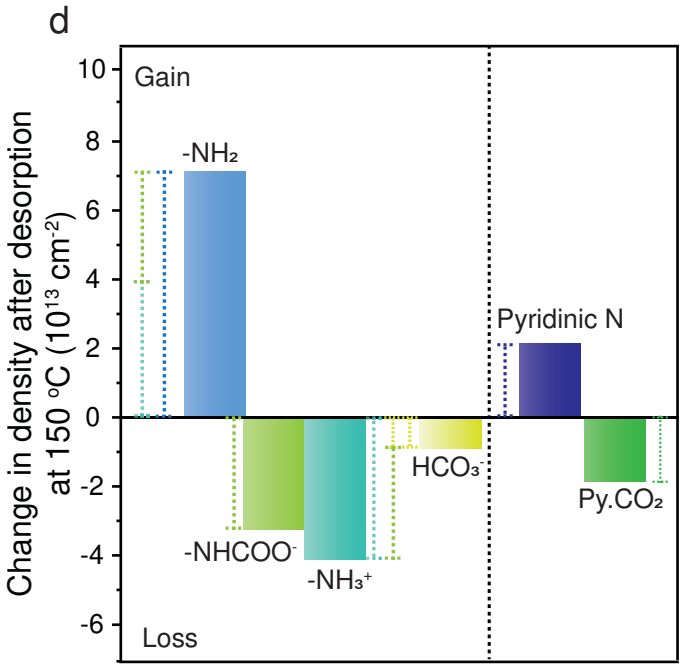
d
Gain
-NH₂
Pyridinic N
HCO₃⁻
Py.CO₂
-NHCOO⁻
-NH₃⁺
Loss
Change in density after desorption at 150 °C (10¹³ cm⁻²)

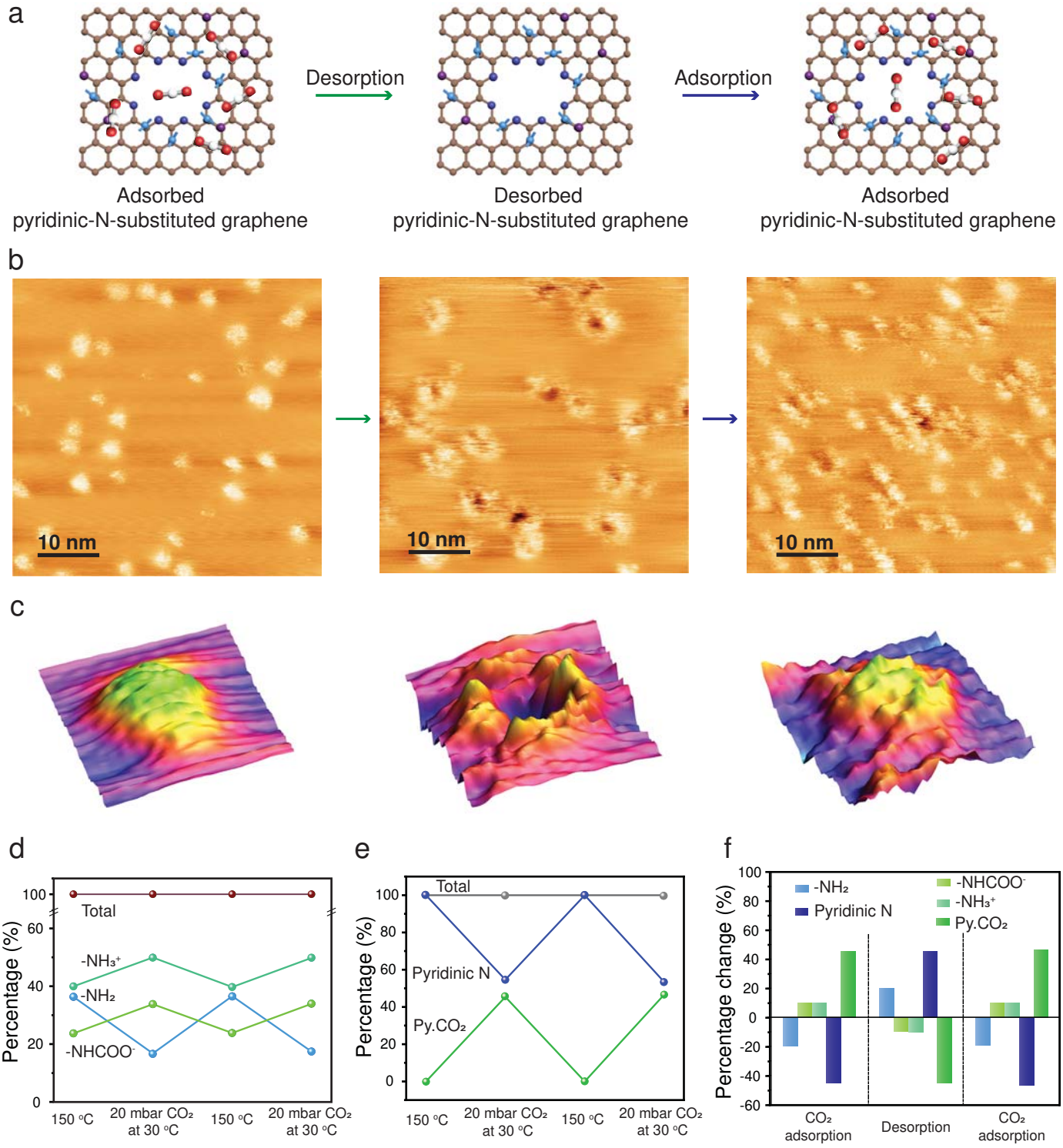
a
Desorption
Adsorption
Adsorbed
pyridinic-N-substituted graphene
Desorbed
pyridinic-N-substituted graphene
Adsorbed
pyridinic-N-substituted graphene
b
10 nm
10 nm
10 nm
c
d
Percentage (%)
Total
-NH3+
-NH2
-NHCOO-
150 °C
20 mbar CO2 at 30 °C
150 °C
20 mbar CO2 at 30 °C
e
Percentage (%)
Total
Pyridinic N
Py.CO2
150 °C
20 mbar CO2 at 30 °C
150 °C
20 mbar CO2 at 30 °C
f
Percentage change (%)
-NH2
Pyridinic N
-NHCOO-
-NH3+
Py.CO2
CO2 adsorption
Desorption
CO2 adsorption

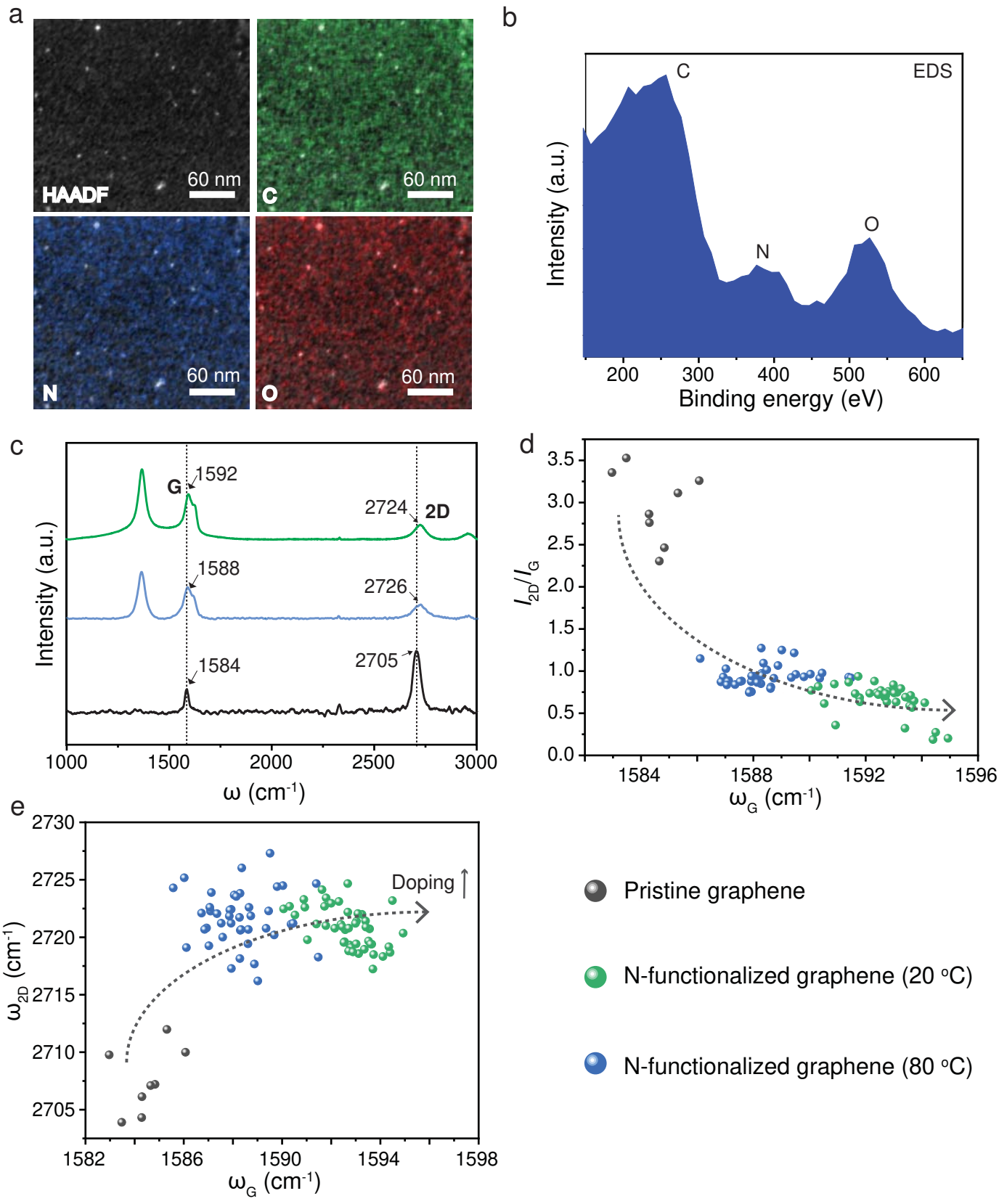
a
HAADF
60 nm
C
60 nm
N
60 nm
O
60 nm
b
EDS
C
N
O
Intensity (a.u.)
200
300
400
500
600
Binding energy (eV)
c
G
1592
2724
2D
1588
2726
1584
2705
Intensity (a.u.)
1000
1500
2000
2500
3000
ω (cm-1)
d
I2D/IG
3.5
3.0
2.5
2.0
1.5
1.0
0.5
0.0
1584
1588
1592
1596
ωG (cm-1)
e
2730
2725
2720
2715
2710
2705
ω2D (cm-1)
Doping
1582
1586
1590
1594
1598
ωG (cm-1)
Pristine graphene
N-functionalized graphene (20 °C)
N-functionalized graphene (80 °C)

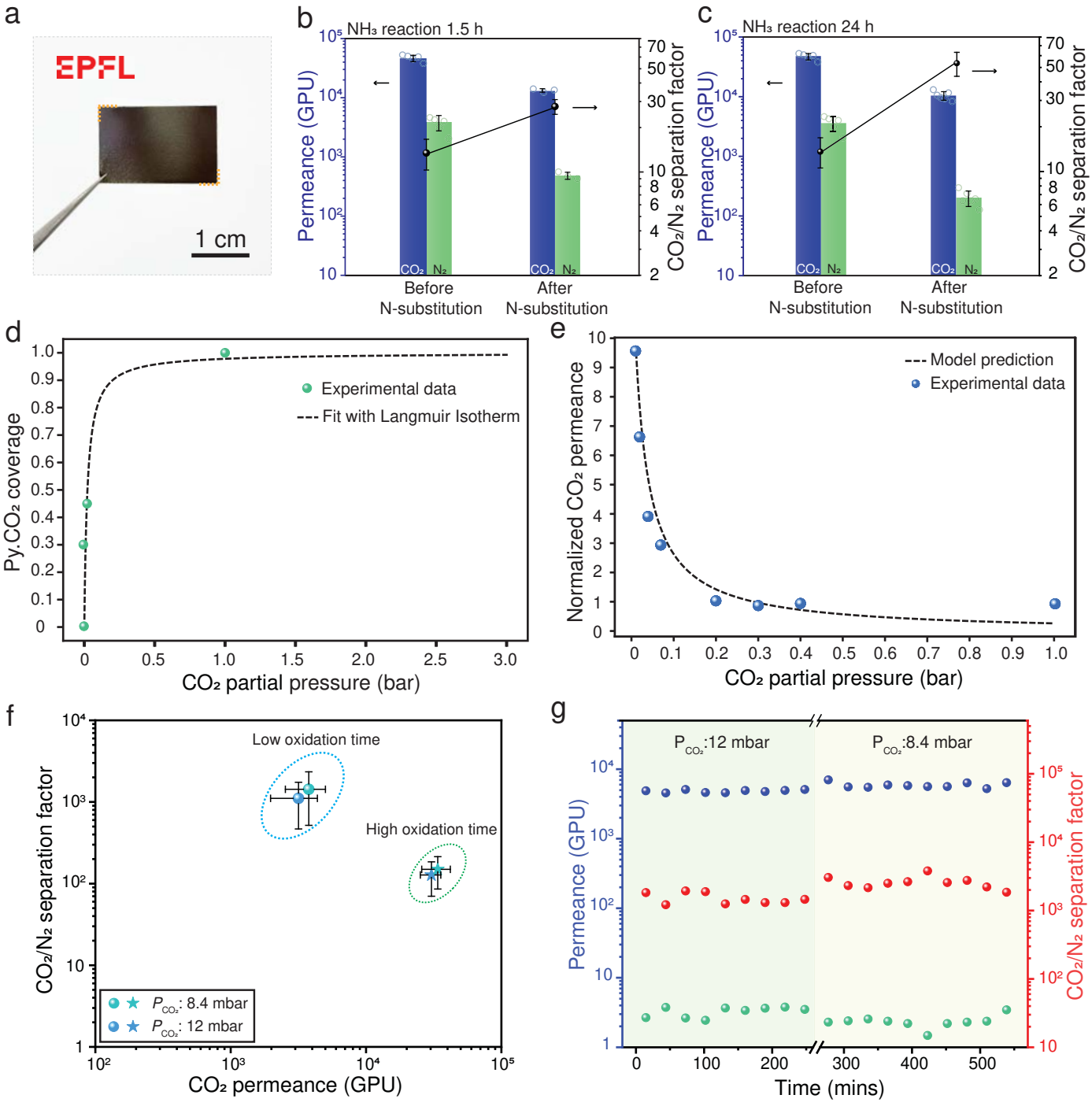
a
EPFL
1 cm
b
NH₃ reaction 1.5 h
Permeance (GPU)
CO₂/N₂ separation factor
CO₂
N₂
Before N-substitution
After N-substitution
c
NH₃ reaction 24 h
Permeance (GPU)
CO₂/N₂ separation factor
CO₂
N₂
Before N-substitution
After N-substitution
d
Py.CO₂ coverage
Experimental data
Fit with Langmuir Isotherm
CO₂ partial pressure (bar)
e
Normalized CO₂ permeance
Model prediction
Experimental data
CO₂ partial pressure (bar)
f
Low oxidation time
High oxidation time
CO₂/N₂ separation factor
P_CO₂: 8.4 mbar
P_CO₂: 12 mbar
CO₂ permeance (GPU)
g
P_CO₂:12 mbar
P_CO₂:8.4 mbar
Permeance (GPU)
CO₂/N₂ separation factor
Time (mins)

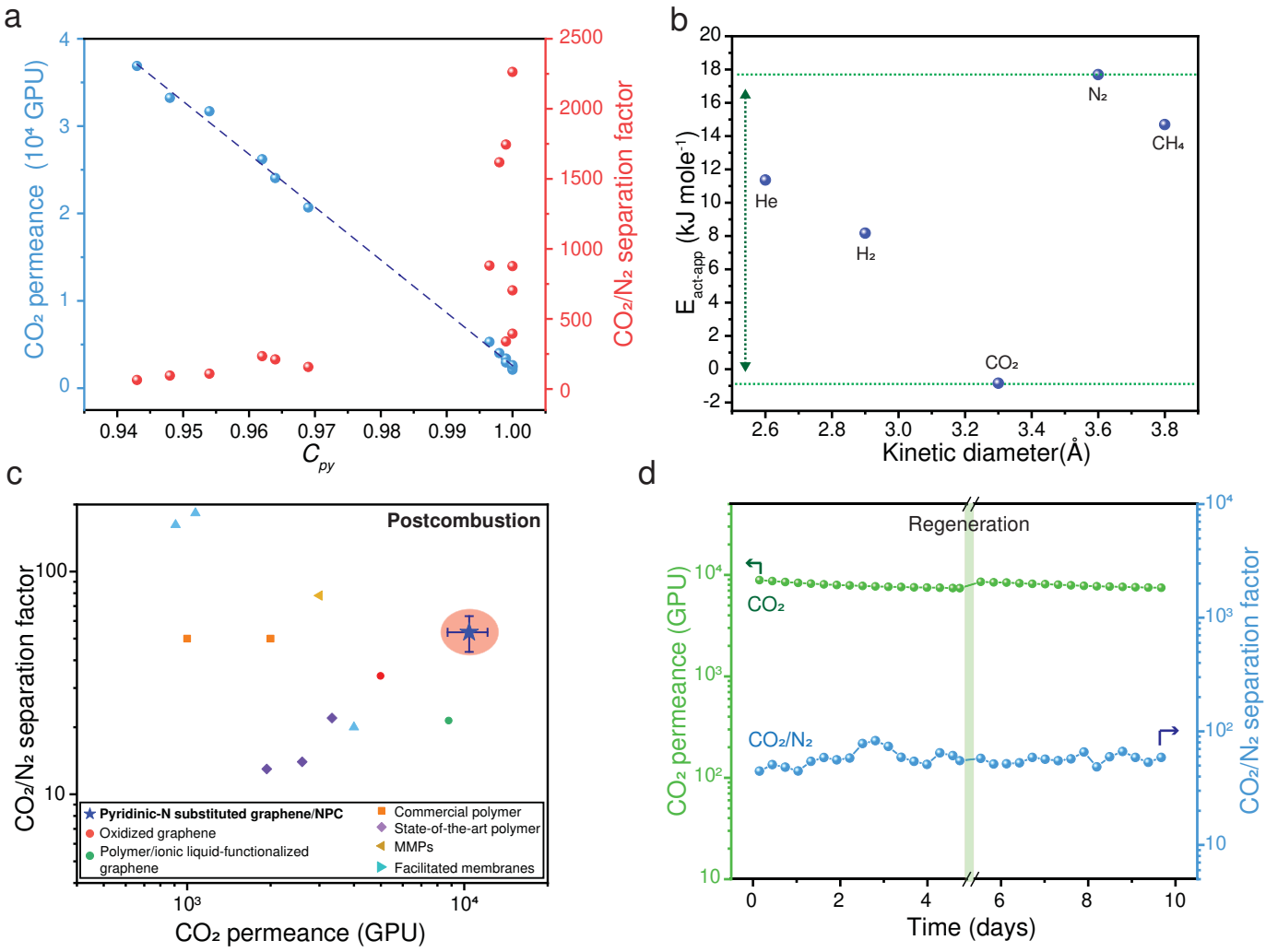
a
CO₂ permeance (10⁴ GPU)
CO₂/N₂ separation factor
C_py
b
E_act-app (kJ mole⁻¹)
Kinetic diameter(Å)
He
H₂
CO₂
N₂
CH₄
c
Postcombustion
CO₂/N₂ separation factor
CO₂ permeance (GPU)
Pyridinic-N substituted graphene/NPC
Oxidized graphene
Polymer/ionic liquid-functionalized graphene
Commercial polymer
State-of-the-art polymer
MMPs
Facilitated membranes
d
Regeneration
CO₂
CO₂/N₂
CO₂ permeance (GPU)
CO₂/N₂ separation factor
Time (days)